Dynamics of diverse polarization singularities in momentum space with far-field interference

Haoqi Luo [1], Liangliang Liu,[1] Zheng Xi,[1,2] Yonghua Lu [1,2,*] and Pei Wang[1,2]

[1]*Department of Optics and Optical Engineering, University of Science and Technology of China, Hefei, Anhui 230026, China*
[2]*Advanced Laser Technology Laboratory of Anhui Province, Hefei, Anhui 230026, China*

Polarization singularities in momentum space, including bound states in the continuum (BICs) and circularly polarized states (CPSs), render great potential in singular and chiral optics. As far-field topological signatures of Bloch modes in photonic crystal slab, the dynamic evolution of the polarization singularities is observed by tuning the geometric parameters of the slab itself. Here, we combine the photonic crystal slab with a reflected multilayer substrate in which interference between the reflected optical field and the upward radiation of the Bloch mode brings us an extra degree of freedom to manipulate the polarization singularities without breaking the structural symmetry. As the polarization singularities evolve with the spacing between the photonic crystal slab and the substrate, the CPSs and extrinsic BICs are both generated from charge reversal of the at-Γ intrinsic BIC and then collide with the off-Γ intrinsic BICs. Importantly, all BICs are topologically protected from splitting throughout the whole dynamic process owing to the preservation of structural symmetry. Our findings suggest an alternative route to pursue ultrahigh-Q CPS resonances and merge diverse BICs, which is potentially applicable in chiral optics, topological photonics, and beam modulation.

I. INTRODUCTION

The optical singularities are widely observed in intensity, phase, and polarization [1–6], which have vast applications ranging from imaging [7] and communication [8] to particle manipulation [9] and nanoscale sensing [10,11]. Spurred by the polarization singularities in real space, bound states in the continuum (BICs) have been confirmed as the integer-charged polarization singularities in momentum space of the Bloch modes in photonic crystal slabs (PCSs) [12,13]. In spite of location within the continuous spectrum of extended states, BICs feature infinite quality factor Q owing to the ill-defined far-field polarization, which have been extensively applied to enhance light-matter interactions [14–16] and construct resonances robust to scattering loss [17,18]. Some other polarization singularities possessing half-integer topological charges are termed elementary singularities [19]. Among them, circularly polarized states (CPSs) only couple with the circularly polarized propagating light in the same handedness [20], which link polarization singularity to chiral optics [21] and facilitate potential applications such as routing the valley exciton emission [22] and chiral lasers [23].

Within this context, generating and tuning various polarization singularities in momentum space are pivotal to advancing the developments of on-chip resonators, nonlocal devices [24,25], and topological and non-Hermitian photonics [26,27]. The dynamics of polarization singularities are generally in connection with the structural symmetry. Previous works [12,17,18] have demonstrated that BICs can be moved without conversion into CPSs when the in-plane inversion and vertical mirror symmetries are preserved. In other words, symmetry breaking is an effective joystick to generate CPSs by decomposing BICs. For instances, pairwise CPSs with identical topological charge and opposite handedness can be generated from the splitting of symmetry-protected BICs [20–24,28], accidental BICs [29], and Friedrich-Wintgen BICs [30]. Recently, CPSs were observed in the PCSs without symmetry breaking [31], but they are also directly associated with BIC splitting because BICs are quite fragile beyond the diffraction limit. Most previous works observed the generation, evolution, and annihilation of the polarization singularities including BIC and CPS by tuning the geometric parameters of the PCS itself. In this case, only intrinsic BICs are involved, and the CPS generations are commonly accompanied by BIC splitting, which places restrictions on the development of some new configurations of polarization singularities. Therefore, it is helpful to introduce another more flexible mechanism to generate the diverse polarization singularities and manipulate them individually.

In this study, we combine the PCS with a reflected multilayer substrate and propose a mechanism of far-field interference to manipulate the diverse polarization singularities in momentum space. This hybrid photonic system (HPS) provides the freedom to modulate the dynamics of polarization singularities by regulating the spacing between the PCS and the multilayer. After elaborately designing the HPS, the extrinsic BICs [32] are observed together with the intrinsic BICs including the symmetry-protected BIC at Γ and accidental BIC at off Γ. Tuning the spacing between the PCS and the multilayer, interesting dynamics of the far-field polarization singularities and intriguing topological configurations are discovered. During the evolution, all BICs are protected from splitting owing to the preserved structural symmetry. The intrinsic BICs play the role of anchor points in momentum space to modulate the CPS trajectories. CPS spawning and

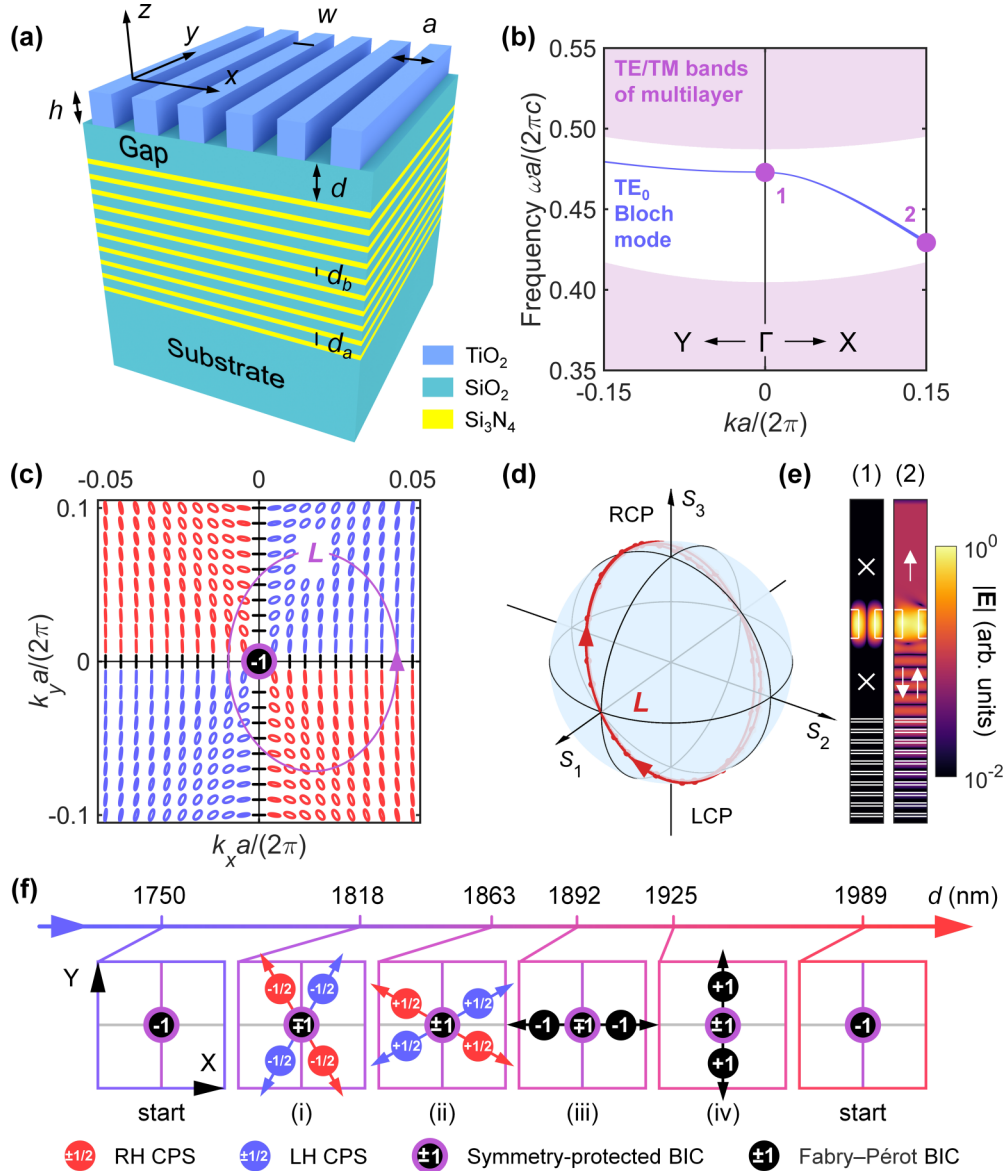*Corresponding author: yhlu@ustc.edu.cn

FIG. 1. Bloch mode existing in the HPS and the intrinsic BIC. (a) Sketch of the PCS-multilayer HPS. (b) Dispersion relation of the TE_0 Bloch mode (blue strip) with the band structure of multilayer as background. The lavender (white) region represents the union of TE and TM bands (polarization-independent band gap). (c) Far-field polarization map at $d = 1750$ nm. The red (blue) ellipses in the second and fourth (first and third) quadrants denote the right (left)-handed elliptic polarizations, and the short black lines for linear polarizations. (d) Trajectory on the shell of the Poincaré sphere mapped from polarization states along the loop L in (c). (e) Electric field distributions in $\log_{10}$ scale of modes marked by the disk 1 [intrinsic BIC, panel (1)] and disk 2 [radiative mode, panel (2)] in (b). (f) Dynamic circle of polarization singularities near the Γ point. The charge conversion from $+1$ (-1) to -1 $(+1)$ is labeled by $\pm1(\mp1)$.

its colliding with the accidental BICs are observed during the dynamic processes, which merely reverse the topological charges without accessional conversion between diverse polarization singularities.

II. BLOCH MODES AND INTRINSIC BICS IN PCS

Figure 1(a) illustrates the HPS composed of a one-dimensional PCS deposited on an all-dielectric multilayer substrate. The PCS consists of a periodic rectangular grating with lattice constant $a = 330$ nm, bar width $w = 165$ nm, and etched from a h-thick TiO_2 slab ($n = 2.58$). The multilayered substrate is made by N pairs of alternating d_a-thick SiO_2 layer

($n_a = 1.46$) and d_b-thick Si_3N_4 layer ($n_b = 2.02$) and a SiO_2 substrate underneath, additionally covered by a d-thick SiO_2 gap layer. The whole structure is immersed in a matching liquid with refractive index of n_a to keep an isotropic environment for the PCS. The multilayer is elaborately designed ($d_a = 163$ nm, $d_b = 65$ nm) with a polarization-independent band gap [white region in Fig. 1(b)]. The nondegenerate fundamental transverse electric (TE_0) Bloch mode of the PCS ($h = 620$ nm) lying within the band gap [blue strip in Fig. 1(b)] guarantees total reflection of the downward leakage of the Bloch mode. As the gap thickness d is set much larger than the attenuation length of evanescent components of the Bloch mode, only far-field interaction should be considered

between the PCS and the multilayer. Hence, the HPS configuration here can be described by a bilayer model possessing C_2 rotation and σ_z mirror symmetries simultaneously (see Appendix A). The characteristics of the eigenmode in the HPS can be investigated by the temporal coupled-mode theory (TCMT) (see Appendixes B and C). The reflected optical field undergoes polarization modulation when it passes through the PCS due to the optical anisotropy of the photonic slab. Therefore, the coherent superposition of the upward radiation of the TE_0 Bloch mode and the reflected light provides an extra degree of freedom to engineer both polarization and intensity of the overall far-field radiation. Regulating phase difference between the superposition waves by changing the gap thickness, we can control the emergence and evolution of polarization singularities in momentum space.

The topological nature of polarization singularity in momentum ($\mathbf{k}_\parallel$) space can be quantitatively described by introducing a topological charge defined as [17]

$$q = \frac{1}{2\pi} \oint_L d\mathbf{k}_\parallel \cdot \nabla_{\mathbf{k}_\parallel} \phi(\mathbf{k}_\parallel), \qquad (1)$$

where $\phi = \frac{1}{2}\mathrm{Arg}(S_1 + iS_2)$ is the orientation angle between the major axis of the projected polarization ellipse and x-axis obtained from the Stokes parameters S_i, and L denotes a counterclockwise closed loop containing the polarization singularity. Figure 1(c) presents the far-field polarization map of TE_0 Bloch mode for the HPS of $d = 1750\,\mathrm{nm}$ with an intrinsic symmetry-protected BIC (i.e., the BIC also exists in the isolated PCS) pinned in the center of the first Brillouin zone (Γ point). We map polarization states along the loop L indicated in Fig. 1(c) onto the shell of the Poincaré sphere to form a closed trajectory [Fig. 1(d)]. Since the topological charge equals half of the winding number for this trajectory around the S_3 axis [31], the winding number of -2 here suggests $q = -1$ for the BIC. The nature of the intrinsic BIC can be further disclosed in its optical field distribution. Comparison of the field distributions between the intrinsic BIC [panel (1)] and ordinary mode [panel (2)] indicates that the electromagnetic mode is perfectly confined inside the PCS at the intrinsic BIC point [Fig. 1(e)]. Therefore, the intrinsic BIC robustly exists without moving or splitting against the substrate changing.

Because topology is a nonlocal property defined by the polarization distribution around the singularity, the topological charge of the intrinsic BIC varies periodically versus the gap thickness d. We exhaustively examine the charge of the intrinsic BIC throughout a whole dynamic circle ranging $d = 1750 - 1989\,\mathrm{nm}$ and find four nontrivial charge reversals. Figure 1(f) schematically illustrates the typical charge configurations, wherein every charge reversal is associated with the charge spawning, such as four CPSs [panels (i) and (ii)] or pairwise BICs in ΓX and ΓY directions [panels (iii) and (iv)], which are governed by the conservation law of topological charge [12].

III. DYNAMICS OF POLARIZATION SINGULARITIES NEAR Γ-POINT

Figures 2(a) and 2(b) present the generation and evolution of CPSs in momentum space by virtue of increasing

d, wherein the right-handed (RH) CPSs are traced by red lines with upward triangles and the left-handed (LH) CPSs by blue lines with downward triangles. Because the in-plane C_2 and mirror (σ_x and σ_y) symmetries maintain in the process, two pairs of CPSs with opposite handedness and identical charge $q = -1/2$ emerge from the Γ point (box $B1$) as $d = 1818\,\mathrm{nm}$. Meanwhile, the at-Γ BIC is topologically protected from splitting [20–24,28–31] but with topological charge reversal (the charge switches from -1 to $+1$) due to the charge conservation (the global charge remains -1). As the spacing continuously enlarges, the four CPSs gradually separate and leave the Γ point and the CPS trajectories are in the same in-plane symmetry (C_2, σ_x, and σ_y) as the HPS. A similar scenario is observed once again at $d = 1863\,\mathrm{nm}$ (box $B3$) except for the reversed charges and the reshaped trajectories. To clarify the topological property of the CPSs, we select the HPSs with $d = 1830\,\mathrm{nm}$ and $d = 1885\,\mathrm{nm}$ (boxes $B2$ and $B4$) to display the far-field maps of polarization orientation angle [Figs. 2(c) and 2(d)]. It is clearly observed that four orientation-angle vortexes possessing half-integer topological charges, denoting the CPSs (red and blue disks), surround the integer-charged intrinsic BIC (black disk with rim).

Considering the material absorption of the PCS, incident light is perfectly absorbed in the same handedness with the CPS at the critical coupling condition, but totally reflected in the opposite handedness, which leads to an outstanding circular dichroism (see Appendix D). We illuminate the HPS with $d = 1885\,\mathrm{nm}$ and absorption coefficient $\mathrm{Im}(n) = -0.0001$ at the matching incident angles and calculate the absorption spectra for right-handed and left-handed circular polarizations [Fig. 2(e)]. Distinct from decomposing BIC to create CPSs [20], the Q factor of CPSs in the HPS relies on the BIC configuration due to simultaneous existence of CPS and BIC. As depicted in Fig. 2(f), four CPSs locate in the high-Q region around the isolated at-Γ BIC, whose Q factors can be enhanced with moving towards the BIC. However, it is impractical for an experiment to push the CPSs very close to the central BIC because the LH and RH CPSs are also too close to be discriminated. Fortunately, the HPS here presents the feasibility to manipulate BICs and CPSs individually. Therefore, we can merge multiple intrinsic BICs by tuning PCS parameter to improve Q factors within a broad wave-vector range, while CPSs are still steerable with d. The combination of CPSs and merging BIC promotes the Q factor of CPS resonances over 10^6, resulting in extremely narrow circular dichroism spectra (see Appendix E).

Further increasing d, pairwise extrinsic BICs due to the Fabry-Pérot effect between the PCS and the reflective substrate spawn in the ΓX ($d = 1892\,\mathrm{nm}$) and ΓY ($d = 1925\,\mathrm{nm}$) directions successively. Figure 3(a) presents the scaling rules of Q factor to show the difference for CPS and BIC spawning situations. The scaling rule of $Q \propto k^{-6}$ along both ΓX and ΓY directions (orange line with circle) manifests that an intrinsic BIC and two emerging extrinsic BICs merge [17]. By contrast, the scaling rule of $Q \propto k^{-2}$ (violet line with triangle) is obtained when four CPSs spawn from the isolated intrinsic BIC, indicating that the CPS generation is unrelated to the BIC splitting. The formation of Fabry-Pérot BICs are attributed to the destructive interference between the direct radiation and the reflected field, when $r_{\mathrm{PCS}}e^{i\delta} = 1$ according
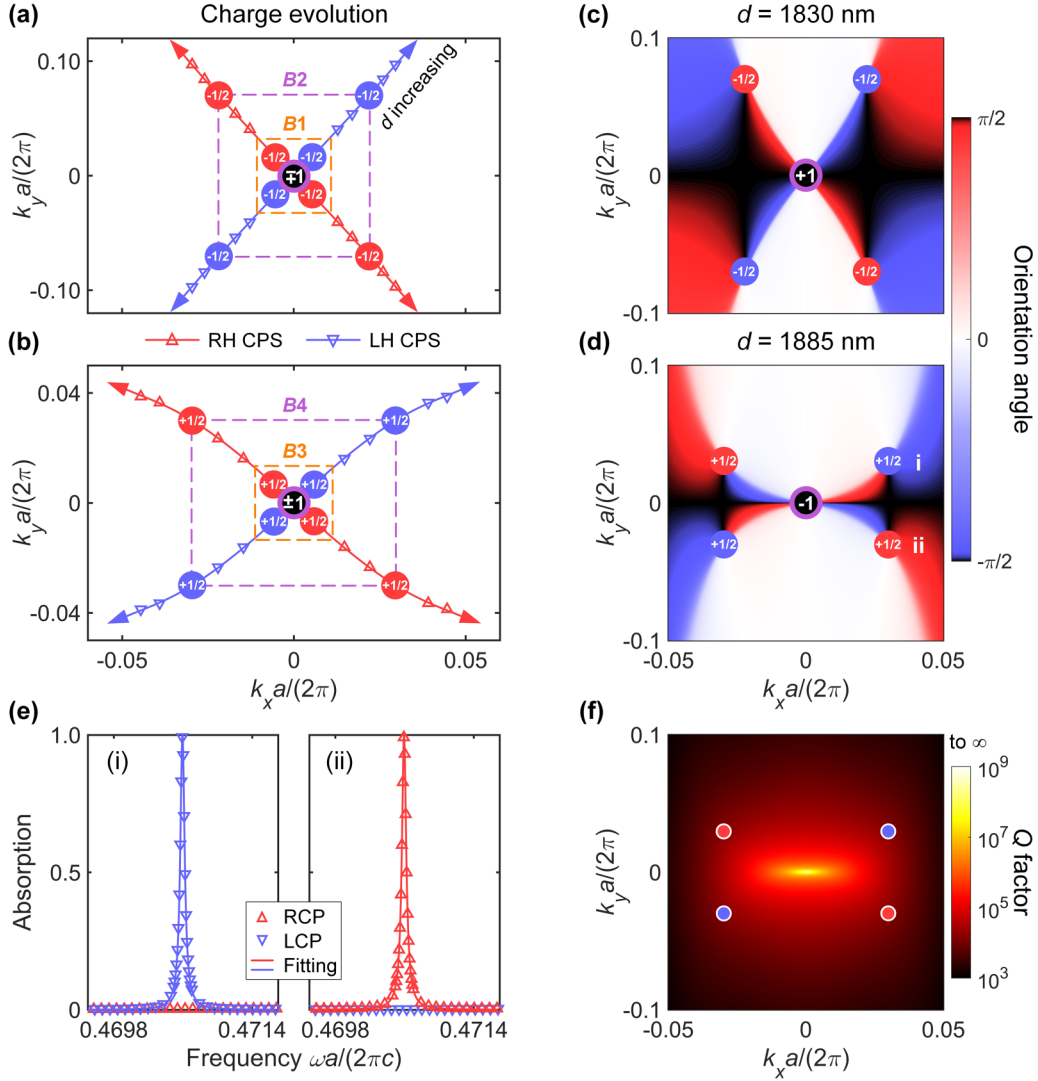
FIG. 2. Characterization and dynamic process of the CPSs. (a),(b) Evolutions of the (a) first and (b) second batches of the CPSs in momentum space as d increases from $d = 1818$ nm to 1840 nm and $d = 1863$ nm to 1910 nm, respectively. The box $B1$ denotes the CPS spawning at $d = 1818$ nm and box $B3$ for $d = 1863$ nm. (c), (d) Far-field polarization-orientation-angle maps at (c) $d = 1830$ nm (box $B2$) and (d) $d = 1885$ nm (box $B4$). (e) Absorption spectra [Im(n) $= -0.0001$] when $d = 1885$ nm under the illuminations of right- and left-handed circularly polarized light with the in-plane wave vectors $\mathbf{k}_{\parallel}a/(2\pi) = (-0.03, -0.03)$ [panel (i)] and $(-0.03, 0.03)$ [panel (ii)], corresponding to the CPSs i and ii shown in (d) respectively. The solid lines denote the results of the Lorenz fitting. (f) CPS configuration at $d = 1885$ nm with Q-factor map as background.

to TCMT (see Appendix C). Here, δ is the phase lag determined by d, and complex coefficient r_{PCS} obtained from the PCS scattering matrix is generally diverse in the ΓX and ΓY directions due to the form birefringence, resulting in different critical gaps for Fabry-Pérot BIC spawning. As d enlarges, the Fabry-Pérot BICs leave the Γ point along high symmetry directions ΓX or ΓY. Figure 3(b) gives the distributions of both the Q factor [panel (i)] and far-field polarization orientation angle [panel (ii)] when $d = 1910$ nm. A pair of off-centered bright spots corresponding to the Fabry-Pérot BICs are observed in the Q-factor map and their topological charges ($q = -1$) are depicted explicitly by the polarization-orientation-angle vortexes. As d increases to 1930 nm, pairwise Fabry-Pérot BICs moving along both the ΓX and ΓY directions are highlighted by the four off-centered bright spots in the Q-factor map [panel (i) in Fig. 3(c)]. The comparison between panels (ii) in Figs. 3(b) and 3(c) distinctly illustrates the charge reversal for the central intrinsic BIC and the global charge conservation during the BIC spawning procedure. We have to point out that the dynamics of Fabry-Pérot BICs depending on the spacing d offer additional flexibility in merging diverse BICs. More importantly, by adding extrinsic BICs into the conventional merging process involving only intrinsic BICs, the Q factor can be further boosted according to the improved scaling rule of $Q \propto k^{-10}$ (see Appendix F).

IV. DYNAMICS OF POLARIZATION SINGULARITIES AT OFF-Γ POINTS

Finally, we demonstrate that the interference mechanism also works at off-Γ points to control the dynamics of polarization singularities. Without loss of generality, we calculated
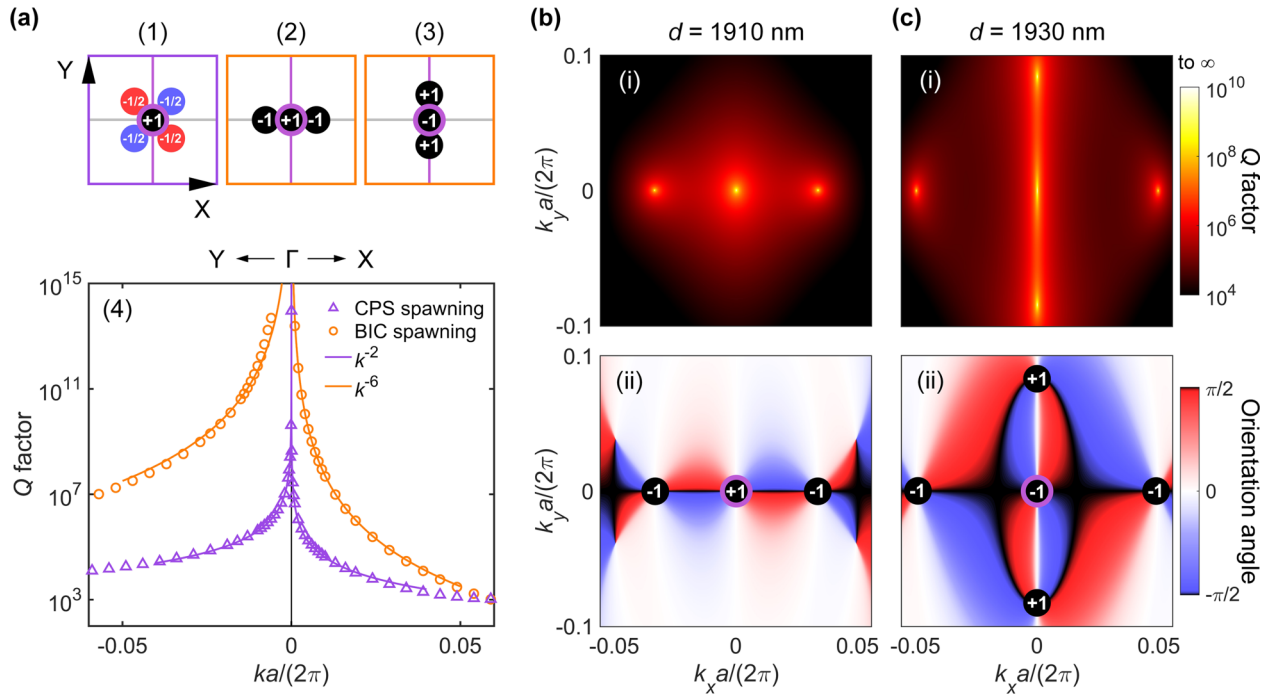
FIG. 3. Dynamic process of the extrinsic BICs and comparison with the CPSs. (a) Sketch of the charge configurations for CPS spawning [$d = 1818$ nm, panel (1)], BIC spawning in ΓX [$d = 1892$ nm, panel (2)], and ΓY [$d = 1925$ nm, panel (3)] directions. Panel (4) plots the Q factor versus Bloch vector for the above scenarios. The circles and triangles represent the numerical results and lines for fitting results. (b), (c) Distributions of both Q factor [panel (i)] and polarization orientation angle [panel (ii)] in momentum space when (b) $d = 1910$ nm and (c) $d = 1930$ nm.

the dynamic circle of polarization singularities around the off-Γ intrinsic accidental BICs for a HPS with $h = 680$ nm. Considering the σ_y mirror symmetry of the HPS, we concentrate on the right semimomentum space for simplicity. As shown in Fig. 4(a), the accidental BIC undergoes a four-time topological charge reversal in a dynamic circle as happens for the symmetry-protected BIC [Fig. 1(f)], yet the underlying mechanisms are different except for the fourth reversal [panel (iv)] caused by Fabry-Pérot BIC spawning. Figure 4(b) displays the charge evolution for the first charge reversal in an enlarged view. Two CPSs with $q = +1/2$ and opposite handedness spawned from the at-Γ intrinsic BIC gravitate to the extra anchor point acted by the off-Γ accidental BIC and then collide with the accidental BIC leading to the charge reversal for all involved singularities. The dynamic process for the second charge reversal behaves in almost the same ways as the first except that charge is switched for the BIC from $+1$ to -1 and for the CPSs from $-1/2$ to $+1/2$ [Fig. 4(c)]. For better understanding, the far-field polarization-orientation-angle map is also exhibited in Fig. 4(d) just before the second collision ($d = 1840$ nm, line $L1$), indicating that two $-1/2$ charged CPSs approach the $+1$ charged off-Γ accidental BIC from the left. After the collision ($d = 1905$ nm, line $L2$), as depicted in Fig. 4(e), the pair of CPSs bounce off and exchange their charges with the BIC. Similar to the CPS colliding, the $+1$ charged Fabry-Pérot BIC in Fig. 4(e) spawned at the Γ point will also collide with the off-Γ accidental BIC when $d = 1931$ nm, bringing about the third charge reversal [panel (iii) in Fig. 4(a)]. After a pair of $+1$ charged Fabry-Pérot BICs spawning at $d = 1965$ nm [panel (iv) in Fig. 4(a)], the off-Γ

accidental BIC is restored to $q = -1$ and the whole dynamic circle is completed. We emphasize that charge annihilation [18] is prohibited in all collision scenarios despite zero global charge for involved singularities because the existence of intrinsic BIC is immune to gap tuning.

We also inspected the Q factor for the scenarios discussed in panels (ii) and (iii) of Fig. 4(a). As shown in Fig. 4(f), the scaling rule of $Q \propto \Delta k_x^{-2}$ is verified for CPS colliding and $Q \propto \Delta k_x^{-4}$ for BIC colliding, unambiguously proving that no extra BIC arises when the pairwise CPSs merge, distinct from the conventional singularity interconversion [29–31]. Figure 4(g) gives the far-field polarization-orientation-angle map at the end of the dynamic circle ($d = 1980$ nm), wherein all involved singularities are in sight, including the two batches of CPSs and the extrinsic BICs bounced and spawned from the intrinsic BIC anchor, indicating the diversity of polarization singularities in the HPS and an unparalleled degree of freedom in managing far-field polarization and intensity. The ultrahigh-Q chiroptical states and merging diverse BICs can also be extended to off-Γ points for more applications requiring angular selectivity.

V. CONCLUSION

In conclusion, we have demonstrated the generation and manipulation of both the CPS and the BIC with optical interference in HPSs instead of breaking C_2 or σ_z symmetries. Distinct from the reported dynamics based on BIC splitting [20–24,28–31], all BICs here are stable and immune from decomposition owing to the symmetry preservation. The
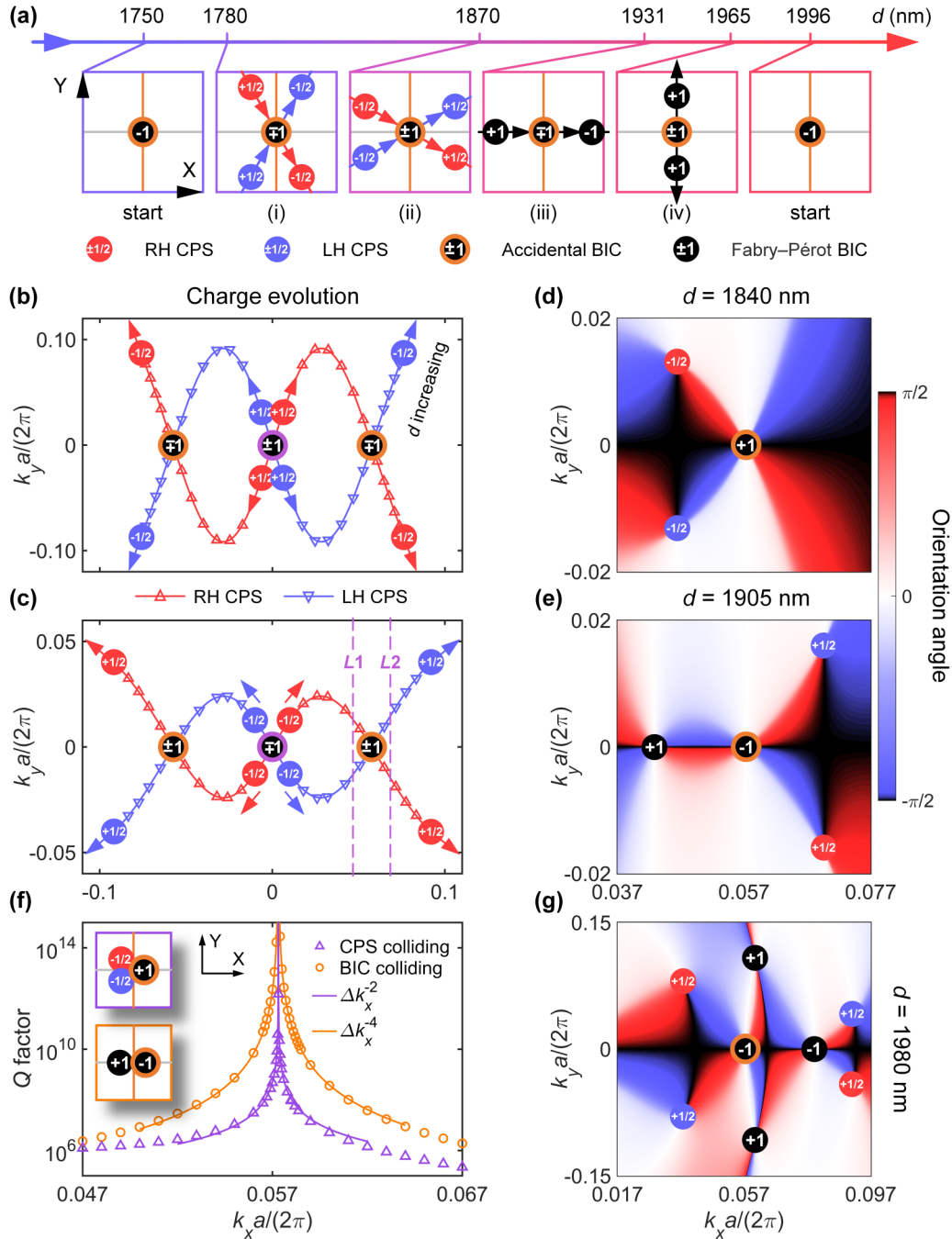
FIG. 4. Dynamic process of polarization singularities at off-Γ points. (a) Dynamic circle of polarization singularities near an off-Γ point $\mathbf{k}_{\mathrm{acc}}a/(2\pi) = (0.057, 0)$, wherein $h = 680$ nm. (b), (c) Evolutions of the (b) first and (c) second batches of the CPSs in momentum space as d increases from $d = 1700$ nm to 1840 nm and $d = 1790$ nm to 1980 nm, respectively. (d), (e) Far-field polarization-orientation-angle maps when (d) $d = 1840$ nm and (e) $d = 1905$ nm [lines $L1$ and $L2$ in (c)]. (f) Q factor versus Bloch vector and its scaling rule for CPS colliding ($d = 1870$ nm) and BIC colliding ($d = 1931$ nm), whose charge configurations are schematically illustrated in the upper and lower insets. The wave-vector difference in scaling rules is defined as $\Delta k_x = k_x - k_{\mathrm{acc},x}$. (g) Far-field polarization-orientation-angle map at $d = 1980$ nm, wherein a pair of CPSs approach the accidental BIC from the left to open up the next dynamic circle.

at-Γ and off-Γ intrinsic BICs act as anchor points to modulate the CPS trajectories in momentum space. As the gap thickness continuously varies, CPSs spawn and then collide with the BIC anchor, which merely results in the reversal of topological charge other than conversion between diverse singularities [20–24,28–31]. Besides the unique CPS configurations, the interference mechanism introduces additional

Fabry-Pérot BICs, which broadens the diversity of BICs in the PCS system. Although the main discussions lie in the framework of preserving both C_2 and σ_z symmetries, the established mechanism with far-field interference remains feasible for symmetry-broken HPSs. Details of the dynamics may be different, but various polarization singularities can also be created and manipulated efficiently (see Appendix G). The extra
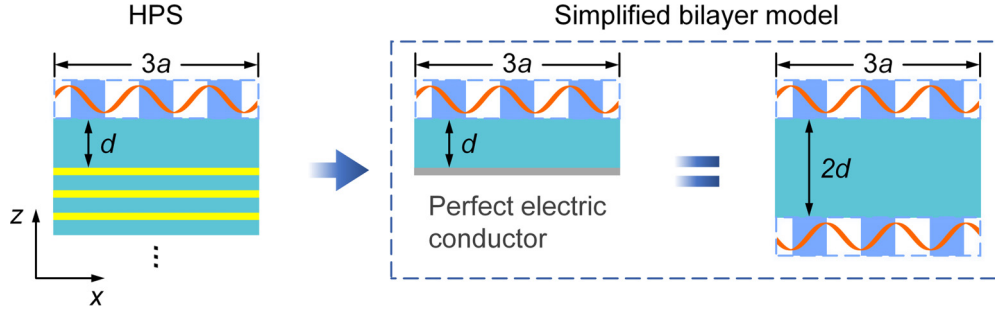
FIG. 5. Schematic illustrations of the HPS (leftmost panel) and the simplified bilayer model (dashed box).

degree of freedom not only enables ultrahigh-Q chiroptical states related to CPSs, promising for biological or chemical sensing, chiral lasing, and narrow-band polarization filters, but also offers additional flexibility to merge diverse BICs, which can enhance light-matter interaction and improve the optical device performance including lasing and nonlinear effect.

ACKNOWLEDGMENT

APPENDIX A: SIMPLIFIED BILAYER MODEL

In this work, we set the gap thickness between the PCS and multilayer ($d > 1750$ nm) much larger than the attenuation length of the evanescent waves (about 160 nm where amplitude decays to -10 dB), therefore, the multilayered substrate works as a perfect mirror to reflect leakage propagating wave of the Bloch modes in the one-dimensional PCS. In this situation, the multilayered substrate can be equivalent to a perfect electric conductor (PEC) in numerical simulation. The optical characteristics of the HPS is finally equivalent to the bilayer model composed of two identical PCSs separated by the gap of thickness $2d$ [Fig. 5(a)], which preserves the in-plane inversion and vertical mirror symmetries.

APPENDIX B: TEMPORAL COUPLED-MODE THEORY MODEL

Temporal coupled-mode theory (TCMT) [28,33] is applied to the HPSs to explain the polarization singularities in momentum space. Considering two open ports for exchanging energy with the external environment of the upper and lower semispaces [Figs. 6(a) and 6(b)] and ignoring material absorption, the dynamic equations of a nondegenerate resonance with in-plane wave vector $\mathbf{k}_{\parallel}$ supported in the PCS can be written as

$$\frac{dA(\mathbf{k}_{\parallel})}{dt} = (i\omega_0 - \gamma_0)A(\mathbf{k}_{\parallel}) + \mathbf{K}^{\mathrm{T}}(\mathbf{k}_{\parallel})\alpha(\mathbf{k}_{\parallel}), \qquad \text{(B1)}$$

$$\beta(\mathbf{k}_{\parallel}) = \mathbf{C}\alpha(\mathbf{k}_{\parallel}) + \mathbf{D}(\mathbf{k}_{\parallel})A(\mathbf{k}_{\parallel}). \qquad \text{(B2)}$$

In these equations, $A(\mathbf{k}_{\parallel})$ is the complex amplitude of the resonance at $\mathbf{k}_{\parallel}$, ω_0 denotes the resonant frequency, and γ_0 represents the decay rate caused by radiation. Considering the two orthogonal radiation channels of s polarization ($\mathbf{s} = \frac{\mathbf{z} \times \mathbf{k}}{|\mathbf{z} \times \mathbf{k}|}$)

and p polarization ($\mathbf{p} = \frac{\mathbf{k} \times \mathbf{s}}{|\mathbf{k} \times \mathbf{s}|}$) in each port, both the input and output waves are 4×1 column vector of $\alpha = (\alpha_s^u, \alpha_s^d, \alpha_p^u, \alpha_p^d)^{\mathrm{T}}$ and $\beta = (\beta_s^u, \beta_s^d, \beta_p^u, \beta_p^d)^{\mathrm{T}}$, wherein the superscript $u(d)$ denotes the upper (lower) port and the subscript $s(p)$ represents the s (p)-polarization channel [Figs. 6(a) and 6(b)]. Accordingly, the coupling coefficients between the resonance and the incoming and outgoing waves are $\mathbf{K} = (k_s^u, k_s^d, k_p^u, k_p^d)^{\mathrm{T}}$ and $\mathbf{D} = (d_s^u, d_s^d, d_p^u, d_p^d)^{\mathrm{T}}$, respectively. Besides the interaction with resonance, the scattering matrix

$$\mathbf{C} = \begin{pmatrix} r_{ss} & t_{ss} & -r_{ps} & t_{ps} \\ t_{ss} & r_{ss} & -t_{ps} & r_{ps} \\ -r_{sp} & t_{sp} & r_{pp} & t_{pp} \\ -t_{sp} & r_{sp} & t_{pp} & r_{pp} \end{pmatrix} \qquad \text{(B3)}$$

describes the direct transmission and reflection through the PCS, which is referred to as the background field in the Fano effect. The scattering matrix $\mathbf{C}$ can be derived by considering the PCS as a uniform anisotropic slab. According to the effective media theory [34], the subwavelength one-dimensional PCS can be equivalent to a uniform slab made of an anisotropic uniaxial media with the effective permittivity of $\varepsilon_{xx} \approx (\frac{f}{\varepsilon_h} + \frac{1-f}{\varepsilon_l})^{-1}$ and $\varepsilon_{yy} = \varepsilon_{zz} \approx f\varepsilon_h + (1-f)\varepsilon_l$, in which $f = w/a$ denotes the fill factor, and $\varepsilon_{h(l)}$ represents the permittivity of TiO_2 (SiO_2). Considering the form birefringence effect of the effective slab, the polarization conversion items including t_{sp}, t_{ps}, r_{sp}, and r_{ps} should be nonzero, different from the discussions for the two-dimensional PCS in previous works [28,35].

In order to discuss eigenmodes of the HPS, the intensity of incident light in the upper semispace is set to zero ($\alpha_s^u = \alpha_p^u = 0$). Because the input wave in the lower semispace originates from the total reflection of the downward radiation by the platform, they follow the phase relation of

$$\left(\alpha_s^d, \alpha_p^d\right)^{\mathrm{T}} = e^{i\delta}\left(\beta_s^d, -\beta_p^d\right)^{\mathrm{T}}, \qquad \text{(B4)}$$

where the phase shift $\delta = -2k_z d + \pi$ is related to the round-trip propagation inside the gap and total reflection by the multilayered substrate. Because the half-wave loss in reflection only happens for the s-polarized wave, there exists an additional amplitude reversal between the s-polarization and p-polarization channels. Furthermore, considering the preserved up-down mirror symmetry of the PCS, the output coupling coefficient $\mathbf{D}$ can be simplified as

$$\mathbf{D} = (d_s, \sigma_z d_s, d_p, -\sigma_z d_p)^{\mathrm{T}}. \qquad \text{(B5)}$$
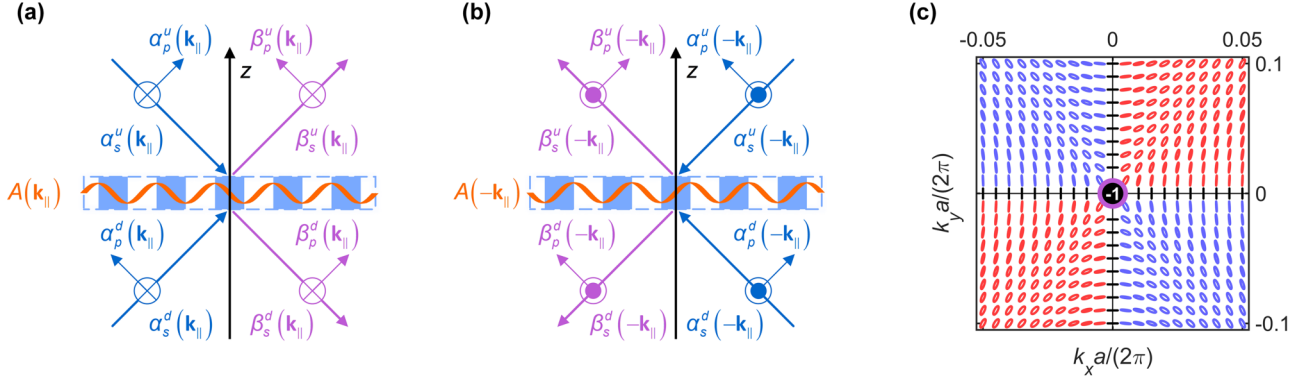
FIG. 6. Temporal coupled-mode theory model. (a),(b) Schematic illustrations of the temporal coupled-mode theory model and definition of polarization vectors in the processes with (a) $\mathbf{k}_\parallel$ and (b) $-\mathbf{k}_\parallel$. The blue and violet lines represent the input and output waves in both s and p polarizations, respectively, and the orange curves indicate the resonance in PCS. (c) Far-field polarization map of the isolated PCS with $h = 620$ nm.

For our concerned TE_0 Bloch mode, the symmetry factor σ_z equals $+1$. Combining Eqs. (B2)–(B5) and using the eigenmode condition ($\alpha_s^u = \alpha_p^u = 0$), we obtain the amplitude of the incident light in the lower semispace:

$$\alpha_s^d = \frac{e^{i\delta}(1 + r_{pp}e^{i\delta})d_s + r_{ps}e^{2i\delta}d_p}{(1 + r_{pp}e^{i\delta})(1 - r_{ss}e^{i\delta}) + r_{sp}r_{ps}e^{2i\delta}}A, \qquad (B6)$$

$$\alpha_p^d = \frac{e^{i\delta}(1 - r_{ss}e^{i\delta})d_p - r_{sp}e^{2i\delta}d_s}{(1 + r_{pp}e^{i\delta})(1 - r_{ss}e^{i\delta}) + r_{sp}r_{ps}e^{2i\delta}}A. \qquad (B7)$$

Inserting Eqs. (B6) and (B7) into Eq. (B2), we obtain the amplitudes of the overall radiation for the Bloch modes in the HPS:

$$\begin{pmatrix} \beta_s^u \\ \beta_p^u \end{pmatrix} = (\mathbf{M} + \mathbf{I})\begin{pmatrix} d_s \\ d_p \end{pmatrix}A = \begin{pmatrix} m_{ss} + 1 & m_{ps} \\ m_{sp} & m_{pp} + 1 \end{pmatrix}\begin{pmatrix} d_s \\ d_p \end{pmatrix}A, \qquad (B8)$$

where

$$m_{ss} = \frac{t_{ss}e^{i\delta}(1 + r_{pp}e^{i\delta}) - t_{ps}r_{sp}e^{2i\delta}}{(1 + r_{pp}e^{i\delta})(1 - r_{ss}e^{i\delta}) + r_{sp}r_{ps}e^{2i\delta}},$$

$$m_{ps} = \frac{t_{ps}e^{i\delta}(1 - r_{ss}e^{i\delta}) + t_{ss}r_{ps}e^{2i\delta}}{(1 + r_{pp}e^{i\delta})(1 - r_{ss}e^{i\delta}) + r_{sp}r_{ps}e^{2i\delta}},$$

$$m_{sp} = \frac{t_{sp}e^{i\delta}(1 + r_{pp}e^{i\delta}) - t_{pp}r_{sp}e^{2i\delta}}{(1 + r_{pp}e^{i\delta})(1 - r_{ss}e^{i\delta}) + r_{sp}r_{ps}e^{2i\delta}},$$

$$m_{pp} = \frac{t_{pp}e^{i\delta}(1 - r_{ss}e^{i\delta}) + t_{sp}r_{ps}e^{2i\delta}}{(1 + r_{pp}e^{i\delta})(1 - r_{ss}e^{i\delta}) + r_{sp}r_{ps}e^{2i\delta}}.$$

By setting the z component to zero, the projected amplitudes of radiation are written as

$$\left(\beta_{s'}^u, \beta_{p'}^u\right)^{\mathrm{T}} = \left(\beta_s^u, \beta_p^u \cos\theta\right)^{\mathrm{T}}, \qquad (B9)$$

where $\theta = \arcsin(\frac{|\mathbf{k}_\parallel|}{|\mathbf{k}|})$ is the angle between the radiation and the z axis, $\mathbf{s}' = \frac{\mathbf{z} \times \mathbf{k}_\parallel}{|\mathbf{z} \times \mathbf{k}_\parallel|}$ and $\mathbf{p}' = \frac{\mathbf{z} \times \mathbf{s}'}{|\mathbf{z} \times \mathbf{s}'|}$ are the projected polarization vectors. Based on the two projected amplitudes, the Stokes parameters used to describe the far-field polarization

states are obtained by

$$S_0 = |\beta_{s'}^u|^2 + |\beta_{p'}^u|^2, \qquad S_1 = |\beta_{s'}^u|^2 - |\beta_{p'}^u|^2,$$

$$S_2 = 2\mathrm{Re}\left(\beta_{s'}^{u*}\beta_{p'}^u\right), \qquad S_3 = 2\mathrm{Im}\left(\beta_{s'}^{u*}\beta_{p'}^u\right). \qquad (B10)$$

It can be observed from Eq. (B8) that the far-field polarization states of HPS are determined by the interference between the original radiation of PCS itself and the reflected optical field modulated by transfer matrix $\mathbf{M}$. Figure 6(c) presents the far-field polarization map for the isolated PCS, wherein the original radiation field are elliptically polarized with the nonzero s-polarized and p-polarized components expect for the Γ-point and two high-symmetry lines. Therefore, according to Eq. (B8), diverse polarization states can be constructed there by engineering the transfer matrix $\mathbf{M}$. Tuning gap thickness is an effective method to implement this concept, while the PCS parameters are fixed.

For instance, we select a specific point of $\mathbf{k}_\parallel a/(2\pi) = (0.03, 0.03)$ in momentum space [position of the left-handed CPS in the first quadrant of Fig. 2(d)] to simulate the S_3 parameter versus the gap d using the finite element method (FEM) [solid line in Fig. 7(a)]. The S_3 value can be significantly modified and approaches -1 periodically as the gap d increases, which indicates the cyclic emergence of the left-handed CPS. Moreover, we also calculate the S_3 parameter by utilizing Eqs. (B8)–(B10) [circles in Fig. 7(a)], wherein $\mathbf{C}$ is established by calculating the scattering matrix for a uniform anisotropic uniaxial slab with the identical thickness as the PCS. The theoretical result of TCMT is in excellent agreement with the numerical simulation. We further count the gap thicknesses at which the CPSs arise [Fig. 7(b)]. The critical gap increases linearly with the CPS order, which quantitatively validates the periodicity in the emergence of the CPS.

APPENDIX C: FORMATION OF EXTRINSIC BICS

The far-field radiation of the TE_0 Bloch modes along the high-symmetry lines in momentum space (i.e., ΓX and ΓY directions) is s polarized [black solid lines in Fig. 6(c)]. Consequently, no polarization conversion occurs in the direct scattering process because polarization of the incident light in the lower half-space is strictly perpendicular or parallel
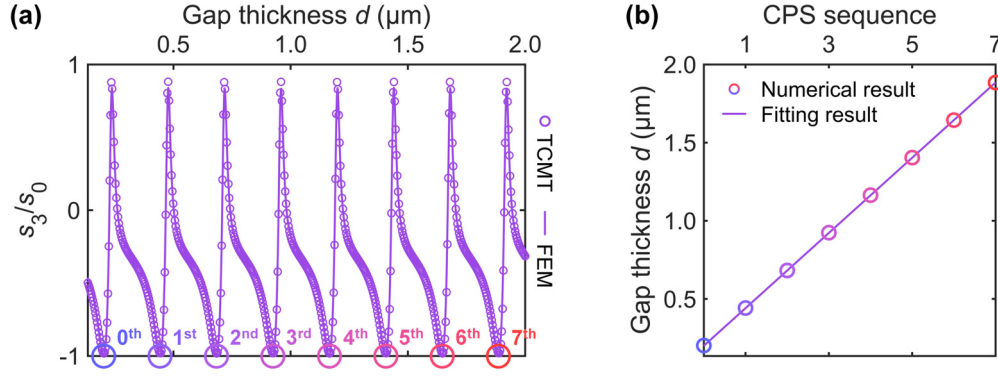
FIG. 7. Characterization of the CPSs and verification by the TCMT model. (a) Normalized S_3 parameter of the radiation for the HPS versus the gap d, calculated at the point of $\mathbf{k}_\parallel a/(2\pi) = (0.03, 0.03)$, corresponding to the LH CPS i in Fig. 2(d). The circles denote the theoretical result calculated by utilizing TCMT and the solid line for the numerical result from FEM simulation. (b) Critical gaps where the CPSs emerge against their mode orders. The solid line denotes the linear fitting with the slope of π/k_z.

to the anisotropy axis of the effective slab. Putting all these conditions into Eq. (B8), we obtain

$$\beta_s^u = \left(\frac{t_{ss}e^{i\delta}}{1 - r_{ss}e^{i\delta}} + 1 \right) d_s A. \tag{C1}$$

By setting radiation intensity to zero, $|\beta_s^u| = 0$, we get the eigenequation of the Fabry-Pérot (extrinsic) BIC:

$$r_{\text{PCS}}e^{i\delta} = 1, \tag{C2}$$

wherein $r_{\text{PCS}} = r_{ss} - t_{ss}$. Considering energy conservation in the direct scattering process of the lossless PCS, the scattering matrix is unitary, i.e., $\mathbf{CC}^\dagger = \mathbf{I}$, and then we have $|r_{\text{PCS}}| = 1$. Due to the form birefringence effect for the PCS, phases of the complex coefficient r_{PCS} are generally different in the ΓX and ΓY directions. Hence, Fabry-Pérot BICs along ΓX and ΓY spawn at different gap thicknesses.

Next, we investigate the resonant frequency and decay rate of the Fabry-Pérot BIC mode by using TCMT. Considering that all incident waves are absent for the PCS, the amplitude of resonance decays exponentially because of the energy dissipation into radiation channels, which can be written as

$$\frac{d|A|^2}{dt} = -\beta^\dagger \beta. \tag{C3}$$

Combining Eqs. (B2) and (C3), we obtain the relation between the output coupling coefficient and the decay rate:

$$\mathbf{D}^\dagger \mathbf{D} = 2\gamma_0. \tag{C4}$$

Then, we assume the time-reversed process for the above situation, that is, the amplitude of resonance $A(-\mathbf{k}_\parallel) = A^*(\mathbf{k}_\parallel)$, grows exponentially without any leakage when the PCS is illuminated by the time-reversed field of the original radiation $\alpha(-\mathbf{k}_\parallel) = (-\mu_z \otimes \mathbf{I})\mathbf{D}^*(\mathbf{k}_\parallel)A^*(\mathbf{k}_\parallel)$, where μ_i is the Pauli matrix. Notably, the $\mathbf{s}$ direction is flipped by the time-reversed operation because it depends on the in-plane wave vector [Figs. 6(a) and 6(b)]. Combining these conditions with Eqs. (B1), (B2), and (C4), we prove that the time-reversed transformation imposes a universal constraint on the relation between the scattering matrix $\mathbf{C}$ and the output (input) coupling coefficient:

$$\mathbf{K}(\mathbf{k}_\parallel) = (-\mu_z \otimes \mathbf{I})\mathbf{D}(-\mathbf{k}_\parallel), \tag{C5}$$

$$\mathbf{C}(-\mu_z \otimes \mathbf{I})\mathbf{D}^*(\mathbf{k}_\parallel) + \mathbf{D}(-\mathbf{k}_\parallel) = 0. \tag{C6}$$

Equation (C6) indicates that the far-field polarization states of the Bloch modes in the PCS are related to the direct scattering matrix. For example, the radiations are almost linearly polarized in the vicinity of the Γ point for the two-dimensional PCS [35]. However, they are elliptically polarized in our considered one-dimensional PCS owing to the birefringence of the effective media [Fig. 6(c)].

By inserting Eqs. (B6) and (B7) into Eq. (B1) and combining Eqs. (C4)–(C6), we obtain the resonant frequency and decay rate of the eigenmodes supported in the HPS:

$$\omega = \omega_0 - \gamma_0 \text{Im}\left(\frac{r_{ss} + t_{ss}}{e^{-i\delta} - r_{ss}} \right), \tag{C7}$$

$$\gamma = \gamma_0 + \gamma_0 \text{Re}\left(\frac{r_{ss} + t_{ss}}{e^{-i\delta} - r_{ss}} \right). \tag{C8}$$

Substituting the Fabry-Pérot BIC condition [Eq. (C2)] into Eqs. (C7) and (C8), we can finally obtain the eigenfrequency and decay rate of the Fabry-Pérot BIC mode:

$$\omega_{\text{BIC}} = \omega_0 - i\gamma_0 \frac{r_{ss}}{t_{ss}}, \tag{C9}$$

$$\gamma_{\text{BIC}} = 0. \tag{C10}$$

According to Eq. (C8), BICs in the HPS can be classified into two different types. One is the intrinsic BIC corresponding to $\gamma_0 = 0$, which is still existed in the isolated PCS, and the other is the extrinsic BIC arisen from the destructive interference between the upward radiation wave from the Bloch mode and the reflected optical field caused by the multilayered substrate, where the destructive interference condition is $r_{\text{PCS}}e^{i\delta} = 1$. Therefore, as the increment of gap d, the intrinsic BIC is robustly pinned at a specific point in momentum space, whereas the extrinsic BIC can be dynamically tuned.

To demonstrate the dependence on gap thickness for the extrinsic BIC, we performed simulations with FEM to calculate the Q factor at a specific $\mathbf{k}$ point of $\mathbf{k}_\parallel a/(2\pi) = (0.03, 0)$ for the HPS with the varying gap thickness d [solid line in Fig. 8(a)], corresponding to the position of the Fabry-Pérot BIC in the right semispace of Fig. 3(b). The Q value diverges periodically as the gap d increases, indicating the cyclical appearance of the tunable extrinsic BIC. The periodicity is further verified by linear fitting for the critical gaps and BIC
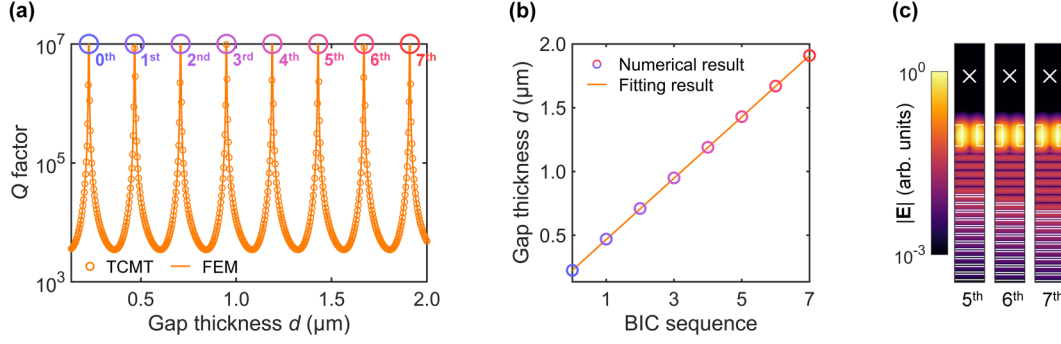
FIG. 8. Characterization of the extrinsic BICs and verification by the TCMT model. (a) Q factor of the TE_0 Bloch mode in the HPS versus the gap d, calculated at the point of $\mathbf{k}_\parallel a/(2\pi) = (0.03, 0)$, corresponding to the extrinsic BIC in the right semispace of Fig. 3(b), where the circles represent the theoretical result calculated by utilizing TCMT and the solid line for the numerical result from FEM simulation. (b) Critical gaps where the extrinsic BICs emerge versus their mode orders. The solid line denotes the linear fitting with the slope of π/k_z. (c) Electric field distributions of the fifth, sixth, and seventh orders of extrinsic BICs.

orders [Fig. 8(b)]. In addition, the Q factor is also theoretically calculated by TCMT according to Eqs. (C7) and (C8) [circles in Fig. 8(a)]. It can be clearly observed in Fig. 8(a) that the TCMT result is completely consistent with the numerical simulation.

For better understanding of the Fabry-Pérot BIC condition, we link Fabry-Pérot BICs with the Fano effect [33] and the Fabry-Pérot cavity. When the PCS is illuminated by the light with frequency ω and in-plane wave vector $\mathbf{k}_\parallel$, the outgoing waves can be obtained by the overall scattering matrix $\mathbf{S}(\mathbf{k}_\parallel)$, which is $\beta(\mathbf{k}_\parallel) = \mathbf{S}(\mathbf{k}_\parallel)\alpha(\mathbf{k}_\parallel)$. By combining Eqs. (B1) and (B2), this matrix is derived as

$$\mathbf{S}(\mathbf{k}_\parallel) = \mathbf{C} + \frac{\mathbf{D}(\mathbf{k}_\parallel)\mathbf{K}^\mathrm{T}(\mathbf{k}_\parallel)}{i(\omega - \omega_0) + \gamma_0}, \tag{C11}$$

which comprises both the direct scattering process, i.e., $\mathbf{C}$, and the indirect radiation way enabled by resonance, i.e., $\frac{\mathbf{D}(\mathbf{k}_\parallel)\mathbf{K}^\mathrm{T}(\mathbf{k}_\parallel)}{i(\omega-\omega_0)+\gamma_0}$. The formation of Fabry-Pérot BIC is actually identical to that of Fano effect. Destructive interference between the direct scattering field (background) and radiation from resonance (indirect pathway) gives rise to the Fabry-Pérot BIC modes (Fano dip in the transmittance). Combining Eqs. (C5), (C6), and (C11), we obtain the amplitude reflectance of the isolated PCS:

$$r_{\mathrm{PCS}} = \frac{i(\omega - \omega_0)r_{ss} - \gamma_0 t_{ss}}{i(\omega - \omega_0) + \gamma_0}. \tag{C12}$$

By substituting the eigenfrequency of Fabry-Pérot BIC [Eq. (C9)] into Eq. (C12), we get the complex reflectance of the PCS: $r_{\mathrm{PCS}} = r_{ss} - t_{ss}$. Because of the unitary scattering matrix $\mathbf{C}$ for the lossless PCS, $|r_{\mathrm{PCS}}| = 1$, indicating that the HPS here is equivalent to a Fabry-Pérot cavity consisting of two perfect mirrors. In this closed cavity, lifetime should be infinitely long for the modes at the resonance condition of $r_{\mathrm{PCS}}e^{i\delta} = 1$, and no leakage field, therefore, can be found out of the cavity. Figure 8(c) presents the electric field distributions for the fifth, sixth, and seventh orders of Fabry-Pérot BICs. Distinct from that all the optical field is confined within the PCS for the intrinsic BIC, standing waves can be explicitly observed inside the gap layer [Fig. 8(c)], which is the typical feature of Fabry-Pérot resonance.

APPENDIX D: CRITICAL COUPLING BETWEEN THE EXTENDED STATES AND CPSs

We employ TCMT to describe the reflection and absorption processes in the PCS-multilayer HPS. The dynamic equations of the nondegenerate resonances supported in the HPS are identical with Eqs. (B1) and (B2), but only the upper port is available here because the lower port is closed by the multilayer. The left- and right-handed circular polarization basis (LCP and RCP) is applied for convenience to discuss the CPSs nearby Γ point. The input and output waves are written as $\alpha = (\alpha_L, \alpha_R)^\mathrm{T}$ and $\beta = (\beta_L, \beta_R)^\mathrm{T}$, respectively, wherein the subscript $L(R)$ denotes the LCP (RCP) channel. Accordingly, the corresponding coupling coefficients with resonance are $\mathbf{K} = (k_L, k_R)^\mathrm{T}$ and $\mathbf{D} = (d_L, d_R)^\mathrm{T}$. Besides the coupling, the direct reflection process is described by a 2×2 matrix:

$$\mathbf{C} = \begin{pmatrix} r_{LL} & r_{RL} \\ r_{LR} & r_{LL} \end{pmatrix}.$$

From reciprocity and time-reversal symmetry [Eqs. (C5) and (C6)], one finds that $\mathbf{K}(\mathbf{k}_\parallel) = \mathbf{D}(-\mathbf{k}_\parallel)$ and $\mathbf{CD}^*(\mathbf{k}_\parallel) = -\mathbf{D}(-\mathbf{k}_\parallel)$. Utilizing the above two conditions, the $\mathbf{S}$ matrix [Eq. (C11)] describing the overall reflection process of the HPS is rewritten as

$$\mathbf{S}(\mathbf{k}_\parallel) = \left(\mathbf{I} - \frac{\mathbf{D}(\mathbf{k}_\parallel)\mathbf{D}^\dagger(\mathbf{k}_\parallel)}{i(\omega - \omega_0) + \gamma_0}\right)\mathbf{C}. \tag{D1}$$

Without loss of generality, we focus on the LH-CPS mode, for which $\mathbf{K} = (k_L, 0)^\mathrm{T}$, $\mathbf{D} = (d_L, 0)^\mathrm{T}$, and $\mathbf{C}$ is a unitary diagonal matrix according to $\mathbf{CD}^*(\mathbf{k}_\parallel) = -\mathbf{D}(-\mathbf{k}_\parallel)$, $\mathbf{CC}^\dagger = \mathbf{I}$. Inserting these conditions into Eq. (D1) and utilizing $\mathbf{D}^\dagger\mathbf{D} = 2\gamma_0$ [Eq. (C4)], we obtain the reflectance for both the LCP and RCP light:

$$R_{LL} = \left| 1 - \frac{2\gamma_0}{i(\omega - \omega_0) + \gamma_0} \right|^2 = 1, \tag{D2}$$

$$R_{RR} = 1, \tag{D3}$$

indicating the total reflection by the lossless HPS.

In the presence of weak material absorption γ_{abs}, R_{LL} cannot equal unity owing to the absorption. According to
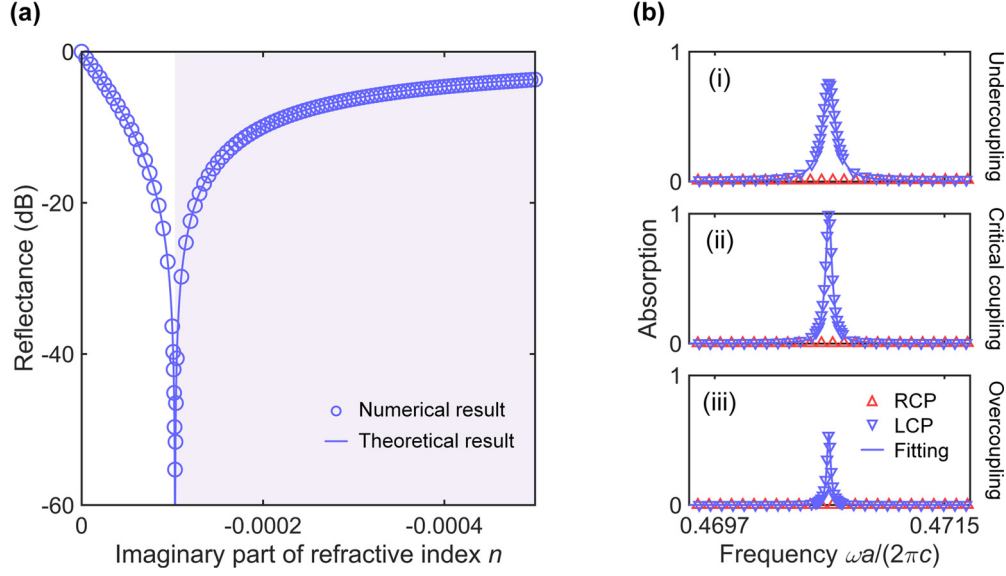
FIG. 9. Critical coupling between the extended states and the CPSs. (a) Reflectance of the PCS-multilayer HPS of $d = 1885$ nm as a function of the imaginary part of refractive index n under the left-handed circularly polarized illumination in the upper semispace with $\mathbf{k}_{\parallel} a/(2\pi) = (-0.03, -0.03)$ and the frequency of 0.4706 c/a, corresponding to the LH CPS i in Fig. 2(d). The circles indicate the numerical result and the line for the theorical result. (b) Absorption spectra of the left and right-handed circularly polarized light at the LH CPS. Im(n) utilized in the panels (i)–(iii) are -3×10^{-4}, -1×10^{-4}, and -2×10^{-5}, respectively, corresponding to the undercoupling [lavender region in (a)], critical coupling [dividing line in (a)], and overcoupling [white region in (a)] regimes.

Eq. (D2), we have

$$R_{LL} = \left| 1 - \frac{2\gamma_0}{i(\omega - \omega_0) + \gamma_{\text{abs}} + \gamma_0} \right|^2. \tag{D4}$$

On resonance, $R_{LL} = \left(\frac{\gamma_{\text{abs}} - \gamma_0}{\gamma_{\text{abs}} + \gamma_0} \right)^2$ reaches zero when $\gamma_{\text{abs}} = \gamma_0$, and γ_{abs} is determined by the imaginary part of the material refractive index. Figure 9(a) shows the reflectance R_{LL} in $\log_{10}$ scale as a function of Im(n). It can be explicitly observed that R_{LL} equals zero at Im(n) = -1×10^{-4} and the numerical result (circles) coincides with the theorical prediction (line) by Eq. (D4).

From Eq. (D4) and using energy conservation, we obtain the absorption spectrum

$$A_L = \frac{4\gamma_{\text{abs}}\gamma_0}{(\omega - \omega_0)^2 + (\gamma_{\text{abs}} + \gamma_0)^2}, \tag{D5}$$

which is a symmetric Lorentz line shape. As depicted in Fig. 9(b), perfect absorption by the resonance occurs at the critical coupling point [$\gamma_{\text{abs}} = \gamma_0$, panel (ii)], and the peak reduces in both undercoupling [$\gamma_{\text{abs}} > \gamma_0$, panel (i)] and overcoupling [$\gamma_{\text{abs}} < \gamma_0$, panel (iii)] regimes. By contrast, RCP light remains total reflection due to the absence of resonance. For the critical case, the Lorentz fit gives the full width at half maximum $\Delta\omega$, and the overall Q_{tot} is obtained by $\omega/\Delta\omega = 7.75 \times 10^3$, which is half of the Q factor (1.5×10^4) for the lossless HPS obtained by eigenmode solver.

APPENDIX E: ULTRAHIGH-Q CHIROPTICAL STATES

Figure 10(a) depicts the realization of the merging BIC, which consists of two intrinsic accidental BICs and one symmetry-protected BIC. The accidental BICs are manip-

ulated by tuning PCS thickness h, while the symmetry-protected BIC is fixed at Γ. As h decreases from 670 nm [panel (1)], the pairwise accidental BICs with $q = +1$ move towards the symmetry-protected BIC with $q = -1$, and the Q factor follows the scaling rule of $Q \propto k_x^{-2}(k_x^2 - k_{\text{BIC}}^2)^{-2}$. When $h = 663.7$ nm [panel (2)], the three intrinsic BICs merge ($k_{\text{BIC}} = 0$) and the scaling rule turns to $Q \propto k_x^{-6}$. Further diminishing h leads to the topological translation [panel (3)]. The accidental BIC pair annihilates accompanied by the charge reversal of the symmetry-protected BIC and the scaling rule finally reduces to $Q \propto k_x^{-2}$. According to the special scaling rule $Q \propto k_x^{-6}$, the Q factor is enhanced within a broad wave-vector range near the merging BIC compared with an isolated BIC [panel (4)].

Then we regulate gap thickness d to manipulate CPSs, while the merging-BIC configuration still holds because the position of intrinsic BIC is immune to gap tuning. As shown in Fig. 10(b), four CPSs locate in the broad ultrahigh-Q region constructed by the merging BIC when $d = 1826$ nm. The Q factor of CPSs is significantly enhanced to the magnitude of 10^6. More generally, the ultrahigh-Q chiroptical states can also be realized far away from the Γ point by arranging CPSs close to an off-Γ merging BIC.

APPENDIX F: BOOSTING Q FACTOR BY HARNESSING EXTRINSIC BICs

Figure 11(a) illustrates the typical topological charge configurations in the merging process with tuning the gap thickness d, in which the PCS thickness h is fixed as 663.7 nm to preserve the merging of intrinsic BICs. The corresponding Q factors and their scaling rules are summarized in Fig. 11(b). In both premerging and postmerging regimes ($d = 1895$ nm
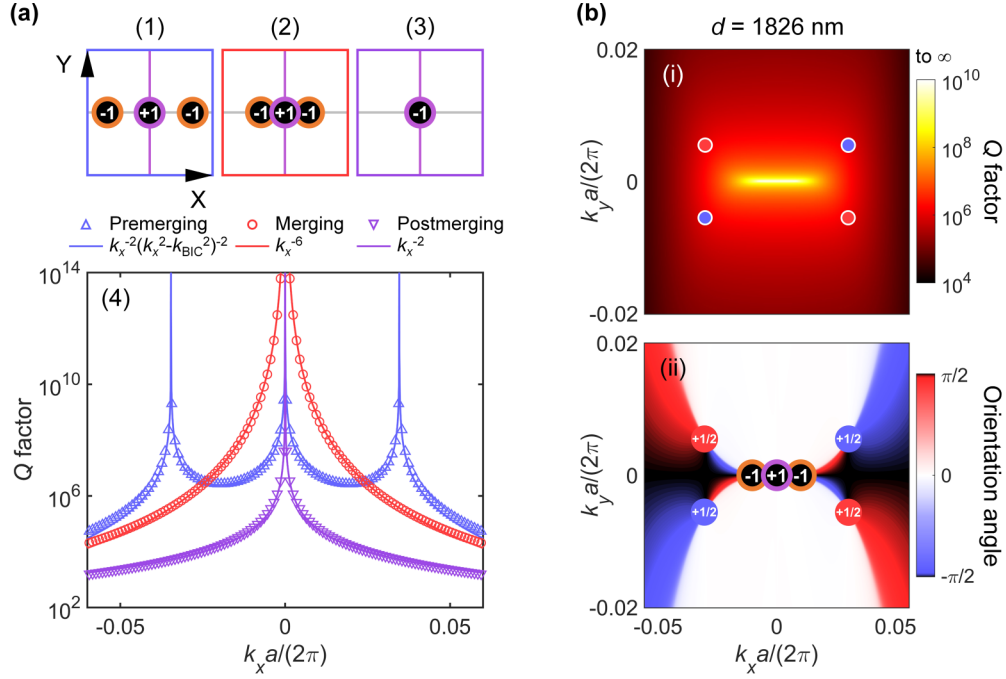
FIG. 10. Ultrahigh-Q chiral states enabled by merging BIC. Panels (1)–(3) in (a) depict the charge configurations for the isolated PCSs with $h = 670$ nm, 663.7 nm, 620 nm, corresponding to the premerging, merging, and postmerging regimes. Panel (4) plots the Q factor and its scaling rule against the wave vector for the three scenarios shown in panels (1)–(3). (b) Distributions of the Q factor [panel (1)] and polarization orientation angle [panel (2)] in momentum space for the PCS-multilayer HPS with $h = 663.7$ nm and $d = 1826$ nm, wherein the four CPSs locate within the ultrahigh-Q region around the central merging BIC.

and $d = 1830$ nm), the Q factors approximatively follow the same scaling rule $Q \propto k_x^{-6}$ in the vicinity of the Γ point. By
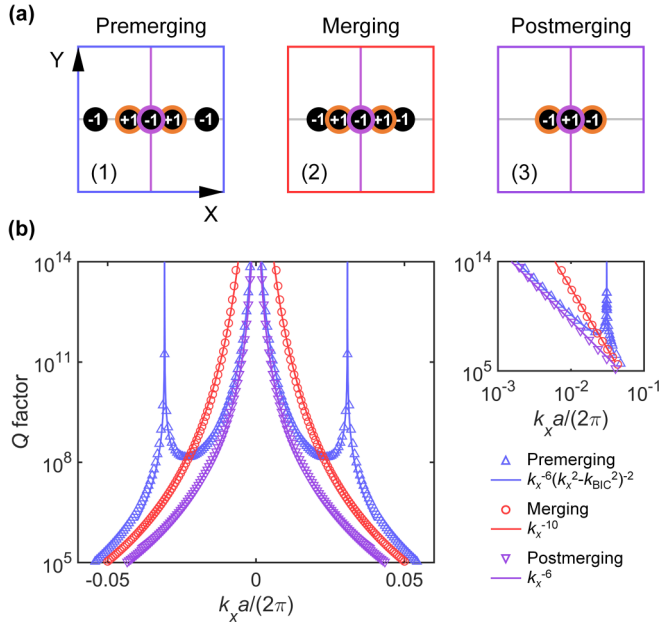

FIG. 11. Boosting Q factor by harnessing extrinsic BICs. Panels (1)–(3) in (a) depict the charge configurations for the HPSs with $d = 1895$ nm, 1876.3 nm, and 1830 nm, corresponding to the premerging, merging, and postmerging regimes. (b) Q factor and its scaling rule versus wave vector for the three scenarios in (a). In calculation, the PCS thickness is fixed as 663.7 nm.

contrast, when the pairwise extrinsic BICs are additionally introduced ($d = 1876.3$ nm), the Q factor grows towards the Γ point much faster than the other two scenarios according to $Q \propto k_x^{-10}$, leading to the significant Q enhancement.

APPENDIX G: DYNAMICS OF POLARIZATION SINGULARITIES IN THE SYMMETRY-BROKEN HPS

As shown in Fig. 12(a), both sidewalls of the bar in PCS are tilted away from the vertical direction with angle $\theta = 85°$. The C_2 and σ_z symmetries of the PCS are broken simultaneously. Therefore, intrinsic BICs are no longer robustly existed. Intriguingly, a different type of dynamic process of polarization singularities is discovered in the HPS by tuning d, which starts from zero topological charge and involves interconversion between the CPS and BIC [Fig. 12(b)]. As $d = 1821$ nm, two pairs of CPSs arise in the vicinity of $\mathbf{k}_\parallel a/(2\pi) = (0.011, \pm 0.102)$ [Fig. 12(c)]. In each pair, CPSs possess opposite topological charges and identical handedness. When d increases, the $-1/2$ charged CPSs move towards the Γ point and the $+1/2$ charged CPSs go outward. When d approaches 1851 nm, the two $-1/2$ charged CPSs with opposite handedness merge and convert into a BIC featuring $q = -1$ at the Γ point [panel (i) in Fig. 12(d)]. Further enlarging d leads to the BIC decomposing, and the emerging two CPSs gradually separate and leave the Γ point [Fig. 12(e)].

The Q-factor map in momentum space is also calculated for the HPS with $d = 1851$ nm [panel (ii) in Fig. 12(d)], in which the extremely bright spot at the Γ point unambiguously verifies the emergence of BIC. The origin of the BIC can further be disclosed from optical field distributions
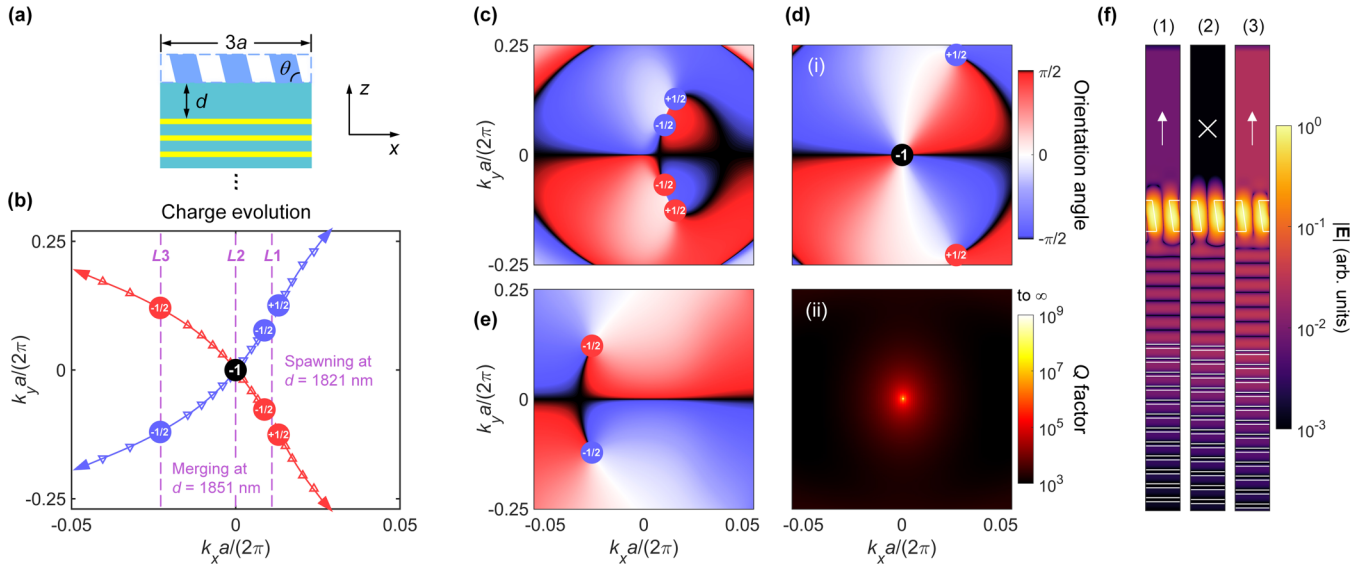
FIG. 12. Dynamics of polarization singularities in the symmetry-broken HPS. (a) Schematic illustration of the HPS wherein both in-plane inversion and vertical mirror symmetries of the PCS are broken. (b) Evolution of the CPSs in momentum space as gap thickness d increases from $d = 1821$ nm to 1960 nm. (c)–(e) Distributions of polarization orientation angle in momentum space for the HPSs with (c) $d = 1821$ nm, (d) $d = 1851$ nm [panel (i)], and (e) $d = 1920$ nm, marked by the dashed lines $L1$, $L2$, and $L3$ in (b), respectively. Panel (ii) in (d) depicts the corresponding Q-factor map. Panels (1)–(3) in (f) present the electric field distributions in $\log_{10}$ scale for the modes at the Γ point in (c)–(e), respectively. In calculation, the PCS thickness is set to 500 nm.

[Fig. 12(f)]. Distinct from the intrinsic BIC with complete field localization in the PCS, the BIC here [panel (2)] is characterized by strong far-field interaction between the PCS and multilayer, which is identical with ordinary modes [panels (1) and (3)]. Thus, although at the Γ point, the BIC is actually a Fabry-Pérot BIC instead of a symmetry-protected BIC.

[1] J. F. Nye, *Natural Focusing and Fine Structure of Light: Caustics and Wave Dislocations* (CRC/Taylor and Francis, London, 1999).

[2] A. M. Yao and M. J. Padgett, Orbital angular momentum: Origins, behavior and applications, Adv. Opt. Photon. **3**, 161 (2011).

[3] J. F. Nye, Polarization effects in the diffraction of electromagnetic waves: The role of disclinations, Proc. R. Soc. Lond. A **387**, 105 (1983).

[4] J. F. Nye, Lines of circular polarization in electromagnetic wave fields, Proc. R. Soc. Lond. A **389**, 279 (1983).

[5] M. Burresi, R. Engelen, A. Opheij, D. van Oosten, D. Mori, T. Baba, and L. Kuipers, Observation of Polarization Singularities at the Nanoscale, Phys. Rev. Lett. **102**, 033902 (2009).

[6] M. R. Dennis, K. O'holleran, and M. J. Padgett, Singular optics: Optical vortices and polarization singularities, Prog. Opt. **53**, 293 (2009).

[7] D. P. Biss, K. S. Youngworth, and T. G. Brown, Dark-field imaging with cylindrical-vector beams, Appl. Opt. **45**, 470 (2006).

[8] J. Wang, J. Liu, S. Li, Y. Zhao, J. Du, and L. Zhu, Orbital angular momentum and beyond in free-space optical communications, Nanophotonics **11**, 645 (2022).

[9] Y. Zhang, J. Shen, C. Min, Y. Jin, Y. Jiang, J. Liu, S. Zhu, Y. Sheng, A. V. Zayats, and X. Yuan, Nonlinearity-induced multiplexed optical trapping and manipulation with femtosecond vector beams, Nano Lett. **18**, 5538 (2018).

[10] Z. Xi, L. Wei, A. J. L. Adam, H. Urbach, and L. Du, Accurate Feeding of Nanoantenna by Singular Optics for Nanoscale Translational and Rotational Displacement Sensing, Phys. Rev. Lett. **117**, 113903 (2016).

[11] S. Nechayev, M. Neugebauer, M. Vorndran, G. Leuchs, and P. Banzer, Weak Measurement of Elliptical Dipole Moments by C-point Splitting, Phys. Rev. Lett. **121**, 243903 (2018).

[12] B. Zhen, C. W. Hsu, L. Lu, A. D. Stone, and M. Soljačić, Topological Nature of Optical Bound States in the Continuum, Phys. Rev. Lett. **113**, 257401 (2014).

[13] H. M. Doeleman, F. Monticone, W. den Hollander, A. Alù, and A. F. Koenderink, Experimental observation of a polarization vortex at an optical bound state in the continuum, Nat. Photon. **12**, 397 (2018).

[14] A. Kodigala, T. Lepetit, Q. Gu, B. Bahari, Y. Fainman, and B. Kanté, Lasing action from photonic bound states in continuum, Nature (London) **541**, 196 (2017).

[15] C. Huang, C. Zhang, S. Xiao, Y. Wang, Y. Fan, Y. Liu, N. Zhang, G. Qu, H. Ji, and J. Han, Ultrafast control of vortex microlasers, Science **367**, 1018 (2020).

[16] Z. Liu, Y. Xu, Y. Lin, J. Xiang, T. Feng, Q. Cao, J. Li, S. Lan, and J. Liu, High-Q Quasibound States in the Continuum for Nonlinear Metasurfaces, Phys. Rev. Lett. **123**, 253901 (2019).

[17] J. Jin, X. Yin, L. Ni, M. Soljačić, B. Zhen, and C. Peng, Topologically enabled ultrahigh-Q guided resonances robust to out-of-plane scattering, Nature (London) **574**, 501 (2019).

[18] M. Kang, S. Zhang, M. Xiao, and H. Xu, Merging Bound States in the Continuum at Off-High Symmetry Points, Phys. Rev. Lett. **126**, 117402 (2021).

[19] W. Liu, W. Liu, L. Shi, and Y. Kivshar, Topological polarization singularities in metaphotonics, Nanophotonics **10**, 1469 (2021).

[20] W. Liu, B. Wang, Y. Zhang, J. Wang, M. Zhao, F. Guan, X. Liu, L. Shi, and J. Zi, Circularly Polarized States Spawning from Bound States in the Continuum, Phys. Rev. Lett. **123**, 116104 (2019).

[21] W. Chen, Q. Yang, Y. Chen, and W. Liu, Extremize Optical Chiralities Through Polarization Singularities, Phys. Rev. Lett. **126**, 253901 (2021).

[22] J. Wang, H. Li, Y. Ma, M. Zhao, W. Liu, B. Wang, S. Wu, X. Liu, L. Shi, and T. Jiang, Routing valley exciton emission of a WS2 monolayer via delocalized Bloch modes of in-plane inversion-symmetry-broken photonic crystal slabs, Light Sci. Appl. **9**, 148 (2020).

[23] X. Zhang, Y. Liu, J. Han, Y. Kivshar, and Q. Song, Chiral emission from resonant metasurfaces, Science **377**, 1215 (2022).

[24] J. Wang, M. Zhao, W. Liu, F. Guan, X. Liu, L. Shi, C. T. Chan, and J. Zi, Shifting beams at normal incidence via controlling momentum-space geometric phases, Nat. Commun. **12**, 6046 (2021).

[25] B. Wang, W. Liu, M. Zhao, J. Wang, Y. Zhang, A. Chen, F. Guan, X. Liu, L. Shi, and J. Zi, Generating optical vortex beams by momentum-space polarization vortices centred at bound states in the continuum, Nat. Photon. **14**, 623 (2020).

[26] W. Chen, Q. Yang, Y. Chen, and W. Liu, Evolution and global charge conservation for polarization singularities emerging from non-Hermitian degeneracies, Proc. Natl. Acad. Sci. USA **118**, e2019578118 (2021).

[27] Q. Song, S. Dai, D. Han, Z. Zhang, C. T. Chan, and J. Zi, PT symmetry induced rings of lasing threshold modes embedded with discrete bound states in the continuum, Chin. Phys. Lett. **38**, 084203 (2021).

[28] T. Yoda and M. Notomi, Generation and Annihilation of Topologically Protected Bound States in the Continuum and Circularly Polarized States by Symmetry Breaking, Phys. Rev. Lett. **125**, 053902 (2020).

[29] X. Yin, J. Jin, M. Soljačić, C. Peng, and B. Zhen, Observation of topologically enabled unidirectional guided resonances, Nature (London) **580**, 467 (2020).

[30] Y. Zeng, G. Hu, K. Liu, Z. Tang, and C.-W. Qiu, Dynamics of Topological Polarization Singularity in Momentum Space, Phys. Rev. Lett. **127**, 176101 (2021).

[31] W. Ye, Y. Gao, and J. Liu, Singular Points of Polarizations in the Momentum Space of Photonic Crystal Slabs, Phys. Rev. Lett. **124**, 153904 (2020).

[32] C. W. Hsu, B. Zhen, S.-L. Chua, S. G. Johnson, J. D. Joannopoulos, and M. Soljačić, Bloch surface eigenstates within the radiation continuum, Light Sci. Appl. **2**, e84 (2013).

[33] S. Fan, W. Suh, and J. D. Joannopoulos, Temporal coupled-mode theory for the Fano resonance in optical resonators, J. Opt. Soc. Am. A **20**, 569 (2003).

[34] A. Poddubny, I. Iorsh, P. Belov, and Y. Kivshar, Hyperbolic Metamaterials, Nat. Photon. **7**, 948 (2013).

[35] C. W. Hsu, B. Zhen, M. Soljačić, and A. D. Stone, Polarization state of radiation from a photonic crystal slab, arXiv:1708.02197.